Journal of Materials Research and Technology 39 (2025) 2079–2093

Contents lists available at ScienceDirect

Journal of Materials Research and Technology

journal homepage: www.elsevier.com/locate/jmrt

Superelasticity and elastocaloric effect of NiTiNb shape memory alloys over a wide working temperature window

Bailiang Qin [a], Ze Pu [a], Changyong Chen [a], Yongyun Zhang [b], K.C. Chan [a,*]

[a] Department of Industrial and Systems Engineering, Research Institute for Advanced Manufacturing, The Hong Kong Polytechnic University, Hong Kong, China
[b] Department of Mechanical Engineering, The University of Hong Kong, Pokfulam Road, Hong Kong, China

ARTICLE INFO

Handling Editor: SN Monteiro

Keywords:
Shape memory alloys
Elastocaloric effect
Superelasticity
Working temperature window

ABSTRACT

Solid-state refrigeration based on the elastocaloric effect is a promising alternative to conventional vapor-compression refrigeration technology due to its environmental friendliness and high energy efficiency. NiTi-based shape memory alloys with a great elastocaloric effect in a wide working temperature window are particularly needed for solid-state refrigeration applications. In this study, a series of $Ni_{50.8\text{-}x}Ti_{49.2}Nb_x$ ($x = 0$, 1, 2, and 3) shape memory alloys were fabricated via arc melting, followed by thermal treatment. The experimental results showed that the martensite transformation temperature decreases with increasing Nb content due to the stabilization of the parent phase by doped Nb atoms. Combining solution strengthening and precipitation strengthening of the Nb addition, the $Ni_{48.8}Ti_{46.2}Nb_2$ alloy demonstrated a significant improvement in the critical stress for martensite transformation and transition strain over a large temperature range of 216–316 K. Meanwhile, it exhibited a large adiabatic temperature change of −10.07 K during rapid stress loading-unloading cycles and a large refrigeration capacity of 3.26 kJ/kg. These findings highlight the high potential of Nb-doping NiTi shape memory alloys for solid-state refrigerants.

1. Introduction

Refrigeration and air-conditioning systems, while essential for modern life, pose environmental challenges through low-energy-efficiency vapor-compression technologies that contribute to global warming [1,2]. The critical need for sustainable cooling has accelerated the development of solid-state technologies such as elastocaloric refrigeration, an eco-friendly alternative that combines high energy efficiency with the elimination of harmful chemical refrigerants [3–5]. The elastocaloric effect is driven by the latent heat released or absorbed during the stress-induced, first-order martensitic transformation, providing a solid-state cooling mechanism [2,4,6]. The advancement of elastocaloric refrigeration is fundamentally governed by the performance of shape memory alloys (SMAs), as these materials serve as the core elements of refrigeration devices [7,8]. With recent progress in elastocaloric material research, several types of SMAs, such as NiTi-based, Cu-based, and NiMn-based alloys, have been found to exhibit substantial elastocaloric effects [9–11]. Among these, binary NiTi SMAs demonstrate outstanding elastocaloric performance to date, including the large adiabatic temperature change (ΔT_{ad}) and isothermal entropy change (ΔS_{iso}) [12–15]. However, there are still limitations for the commercial application of NiTi SMAs as a solid-state refrigerant. These limitations originate from two key challenges: (1) enhancement of service life, particularly fatigue performance and functional stability, and (2) improvement of refrigeration capacity, specifically ΔT_{ad} and the working temperature window [16]. The functional working temperature window is defined by the range of concurrent superelastic and elastocaloric behavior [17,18]. An expanded working temperature window enables stress-induced MT to be triggered under extreme environments, with a considerable ΔT_{ad}. However, current elastocaloric materials normally exhibit a constrained working temperature window; for instance, NiTi SMAs typically operate within a range of only ~30 K, significantly limiting their practical implementation [19]. To meet practical refrigeration demands, SMAs must simultaneously achieve a large, reversible elastocaloric effect and a wide working temperature window.

Several strategies have been developed to improve the working temperature window of SMAs for elastocaloric applications. One is to enhance the yield strength of the matrix, which is higher than the critical stress for stress-induced MT, enabling the matrix to start the MT instead of plastic deformation over a wider temperature range. For instance, nanocrystalline equiatomic NiTi SMAs subjected to severe deformation

---

* Corresponding author.
E-mail address: kc.chan@polyu.edu.hk (K.C. Chan).

https://doi.org/10.1016/j.jmrt.2025.09.207
Received 1 August 2025; Received in revised form 9 September 2025; Accepted 21 September 2025
Available online 22 September 2025

and optimized thermal treatment demonstrate an extended working temperature window of ∼100 K [20]. However, the large volume fraction of the grain boundaries reduces the matrix participation in stress-induced MT, thereby degrading the elastocaloric performance. In addition, it is also reported that the high entropy SMA based on NiTi SMAs exhibits a broad temperature range of 200 K by employing the core effect of severe lattice distortion [21]. Another strategy, elemental alloying of NiTi SMAs, has emerged as an effective approach to improve the working temperature window in the low temperature range of superelasticity and elastocaloric by lowering the phase transformation temperature. For example, nanocrystalline NiTiCo SMAs exhibit a wide operational temperature range from 123 K to 223 K and substantial latent heat by lowering phase transformation temperature, although their high critical stress may compromise energy efficiency [22]. In addition, NiTi-X (X = Co, Cr, Mn, and Fe) strain glass is also able to lower phase transformation temperature by introducing these third elements as point defects to stabilize the parent phase, expanding the superelasticity at lower temperature [23,24].

Among microalloying NiTi-based SMAs, NiTiNb SMAs have garnered significant attention due to their unique eutectic microstructure, as evidenced by the Ni–Ti–Nb ternary phase diagram [25–27]. For instance, Fan et al. [28] studied the microstructure of NiTiNb alloys with varying Ni/Ti ratios, revealing two distinct Nb-containing phases, (1) nanoscale Nb-rich precipitates (≤50 nm) uniformly distributed throughout the matrix, and (2) larger β-Nb precipitates (∼200 nm) concentrated in the eutectic region. Their work demonstrates that these β-Nb precipitates effectively impede MT, lowering the MT start temperature (M_s). Based on the concept of elastic and transformation strain matching, a novel $Ni_{41}Ti_{39}Nb_{20}$ nanocomposite exhibits a unique combination of properties: large elastic strain, low modulus, and high strength [29]. The microstructure, mechanical properties, and superelasticity of porous NiTiNb alloys prepared based on the eutectic reaction were also investigated, revealing that interfacial dislocations and stacking faults accelerated eutectic phase transformation, while rod-like eutectic phases pinned screw dislocations, promoting stress-induced R martensite nucleation [30,31]. Recently, Xi et al. investigated the in-situ alloying of NiTiNb ternary shape memory alloys using laser powder bed fusion (LPBF) with pre-alloyed NiTi powders and element Nb powders, which provides a feasible way to prepare components with complex shapes for elastocaloric application [32–34]. However, a high-volume fraction of the second phase reduces the effective matrix volume participating in martensitic transformation, the matrix volume available for MT, thereby leading to degradation of the elastocaloric effect. While several studies have explored low-Nb alloys, where Nb atoms were used to substitute Ni and Ti simultaneously, to improve the superelasticity and mechanical properties [33,34], the elastocaloric effect performance, such as adiabatic temperature change, latent heat release, functional stability, and working temperature window, of NiTiNb alloys is still unrevealed.

In this study, a series of low Nb content $Ni_{50.8\text{-}x}Ti_{49.2}Nb_x$ (x = 0, 1, 2, and 3) alloys was fabricated via arc melting followed by solution and aging treatments in order to investigate their potential as elastocaloric materials for solid-state refrigeration. Here, Nb substitution for Ni was employed to enhance the thermodynamic stability and yield strength of the austenite phase. The Nb content was restricted to less than 3 at. % to prevent excessive austenite stabilization, which would suppress MT and degrade superelasticity and elastocaloric performance. After optimized thermal treatment, they are expected to exhibit improved mechanical properties and a broader working temperature window without compromising elastocaloric performance. The aged $Ni_{48.8}Ti_{49.2}Nb_2$ alloy presents a synthesis of solution strengthening and precipitate strengthening, yielding significant improvement of both critical stress for stress-induced MT and transition strain with 889.11 MPa and 4.46 %, compared to 248.41 MPa and 4.08 % of the aged $Ni_{50.8}Ti_{49.2}$ alloy. Combining the parent-phase stabilization and strengthened matrix, the working temperature window is expanded to 100 K in the aged $Ni_{48.8}Ti_{49.2}Nb_2$ alloy, which also exhibits an outstanding elastocaloric performance with a maximum adiabatic temperature change of −10.07 K at its peak temperature and a large refrigeration capacity of 3.26 kJ/kg. These findings highlight the potential of NiTiNb alloys for solid-state refrigeration applications.

2. Methodology

Four ingots of $Ni_{50.8\text{-}x}Ti_{49.2}Nb_x$ (x = 0, 1, 2, 3) were prepared by vacuum arc melting in an argon atmosphere using (99.99 wt %) Ni, (99.99 wt %) Ti, and (99.99 wt %) Nb raw materials. Each ingot was remelted six times to ensure homogeneity before being suction-cast into a water-cooling copper crucible with dimensions of 5 × 10 × 60 mm. The cast specimens were first solution-treated at 1223 K for 2 h in a furnace under an argon atmosphere, followed by water quenching, and then aged at 723 K for 4 h.

The microstructure and morphology of the samples were characterized using a scanning electron microscope (SEM, Tescan VEGA3) with energy dispersive spectroscopy (EDS, Oxford). The martensite transformation characteristics were measured by a differential scanning calorimeter (DSC, TA DSC 250) with a constant heating/cooling rate of 10 K/min. For transmission electron microscopy (TEM, JEOL-2100F equipped with an accelerating voltage of 200 kV) investigation, specimens were mechanically ground to around 30 μm thickness, followed by ion milling.

The mechanical properties of the alloys were evaluated using a universal testing machine (Zwick/Roell Z020) equipped with a low-temperature environmental chamber. Two specimen geometries were prepared: cylindrical specimens (3 mm diameter × 6 mm height) and cuboid specimens (3 × 3 × 6 mm) for mechanical and functional characterization. All specimens were mechanically polished to achieve smooth surfaces prior to testing. Compression testing, including both fracture and cyclic measurements, was conducted at a controlled strain rate of $1 \times 10^{-4}\ s^{-1}$ to maintain isothermal conditions. For approaching the adiabatic condition approximation during elastocaloric characterization, a high strain rate of $1 \times 10^{-1}\ s^{-1}$ was implemented across the designated temperature range. The monitoring of the elastocaloric effect, ΔT_{ad}, during the compression process was achieved through synchronized measurements using an Infrared thermography camera (FLIR X8583) and K-type thermocouples (Omega 5 TC-TT-K-40).

3. Results and discussion

3.1. Microstructures

Fig. 1 shows the SEM images of the aged $Ni_{50.8\text{-}x}Ti_{49.2}Nb_x$ (x = 0, 1, 2, 3) alloys (denoted as S0, S1, S2, and S3). Low-magnification images (Fig. 1 (a1) - (d1)) reveal columnar crystal structures with the width of columnar grain exceeding 150 μm in aged S0 and S1 samples, while a smaller grain width in a range of 50–100 μm in aged S2 and S3 (grain boundaries marked by red dashed line). In the binary S0 alloy, massive white needle-like precipitates after aging treatment are distributed in the grain, as shown in Fig. 1 (a2). To identify the precipitates in aged S0 samples, the EDS results (Table 1) of points A (the precipitates) and B (the matrix) in Fig. 1 (a3) indicate a slightly Ni-rich composition in the white precipitates. With 1 at. % Nb addition (S1), these Ni_4Ti_3 precipitates disappeared, replaced by Nb-rich phases distributed randomly (green arrows, Fig. 1 (b2)), confirmed by the elemental mapping on the upper right-hand corner in Fig. 1 (b3). With further increase in the Nb content, the white dendrite-like precipitates appear around the grain boundaries and interiors in the S2 and S3 specimens after aging treatment (blue arrows in Fig. 1 (c1) and (d1)). The element distribution of the white dendrites was investigated by EDS mapping of the selected area in the aged S3 sample. In the figure, it can be confirmed that the white mesh-like dendrite structure is Nb segregation, consistent with prior reports [35,36]. Notably, fine black precipitates were observed

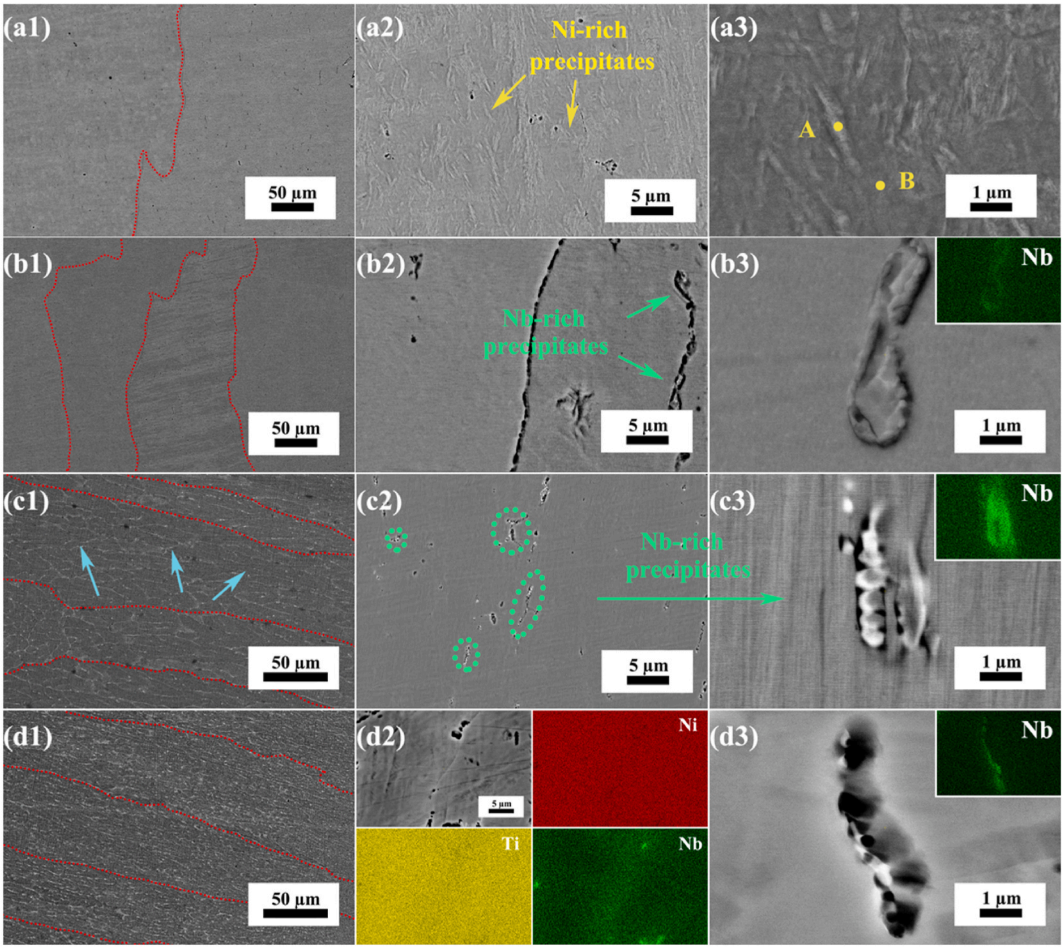

Fig. 1. SEM micrographs and EDS mapping of aged (a1-a3) S0, (b1-b3) S1, (c1-c3) S2, and (d1-d3) S3.

Table 1
Chemical composition of selected points in Fig. 1(a3).

	Ni	Ti
A	51.27	48.76
B	51.09	48.91

along these Nb-rich dendrites, as shown in Fig. 1 (c2). On the observation at higher magnification (Fig. 1 (c3) and (d3)), cellular structure precipitates were detected inside the black precipitates with higher Nb concentration.

Fig. 2 shows TEM characterization of the aged S0 (Fig. 2(a)–(d)) and S3 (Fig. 2(e)–(f)) alloy. In Fig. 2 (a), stripe-like R phases with a length of around hundreds of nanometers were observed in the aged S0 alloy, exhibiting a similar morphology as previously reported work [37,38]. The existence of the R phases indicates the microstructure is undergoing an austenite to R phase transition at RT, which will be further confirmed by the following DSC tests. According to Fig. 2 (c), the SAED pattern confirms the B2 matrix from the $[111]_{B2}$ axis. The reflection spots marked by red at 1/3 positions along $<110>_{B2}$ indicate the existence of the R phase [39]. It is well known that the R phase transformation is attributed to the local elastic strain field around Ni_4Ti_3 precipitates [40, 41]. The needle-like nanoscale Ni_4Ti_3 were observed in the aged S0 sample, which can be confirmed by the corresponding selected area electron diffraction (SAED) as shown in Fig. 2(b) and (c). The double spot halo pattern at 1/7 $<123>_{B2}$ is caused by Ni_4Ti_3 precipitates as marked by the yellow rectangle [39]. The characteristic needle-like Ni_4Ti_3 precipitates were absent in aged S3 alloy due to the modified matrix composition, where Nb doping reduces the Ni/Ti ratio below the precipitate requirement for Ni_4Ti_3 formation [42]. Instead, the Ni_2Ti_4O precipitates were also observed in aged S3 alloy, as confirmed by HRTEM and corresponding FFT (Fig. 2 (d)). In addition, a larger Nb-rich precipitate was observed (Fig. 2 (e)), which is confirmed by corresponding EDS mapping (Fig. 2 (f)), confirming significant Nb segregation in these larger precipitates, which is consistent with the above black precipitates observed in SEM images. The precipitates are probably eutectic β-Nb precipitates as reported by Fan. et al. [43]. According to their work, the eutectic β-Nb phase was observed with 4 at. % Nb addition after solution treatment followed by water quenching. This precipitate evolution demonstrates that doping the Nb element can fundamentally alter the microstructure of NiTi alloys while avoiding the pure β-Nb phases typical of higher Nb compositions.

3.2. Phase transformation behaviour

Fig. 3 presents the thermal-introduced phase transformation behaviour of $Ni_{50.8\text{-}x}Ti_{49.2}Nb_x$ ($x = 1, 2, 3$ at. %) alloys during cooling and heating in a temperature range of 123–423 K with a cooling and heating rate of 10 K/min. The MT starting, peak, and finish temperature (M_s, M_p, and M_f) and AT starting, peak, and finish temperature (A_s, A_p, and A_f) were determined by the tangent method. The thermal hysteresis ΔT_{hys} was calculated as the difference between M_p and A_p. The enthalpy changes $\Delta H_{A\rightarrow M}$ and $\Delta H_{M\rightarrow A}$ of the thermal-introduced MT and AT during the cooling and heating were obtained by integrating the peaks in the DSC curves. The DSC curves in Fig. 3(a–c) show the evolution of the phase transformation behavior of four different samples under as-cast, solution-treatment, and aging conditions, respectively. The as-cast S0

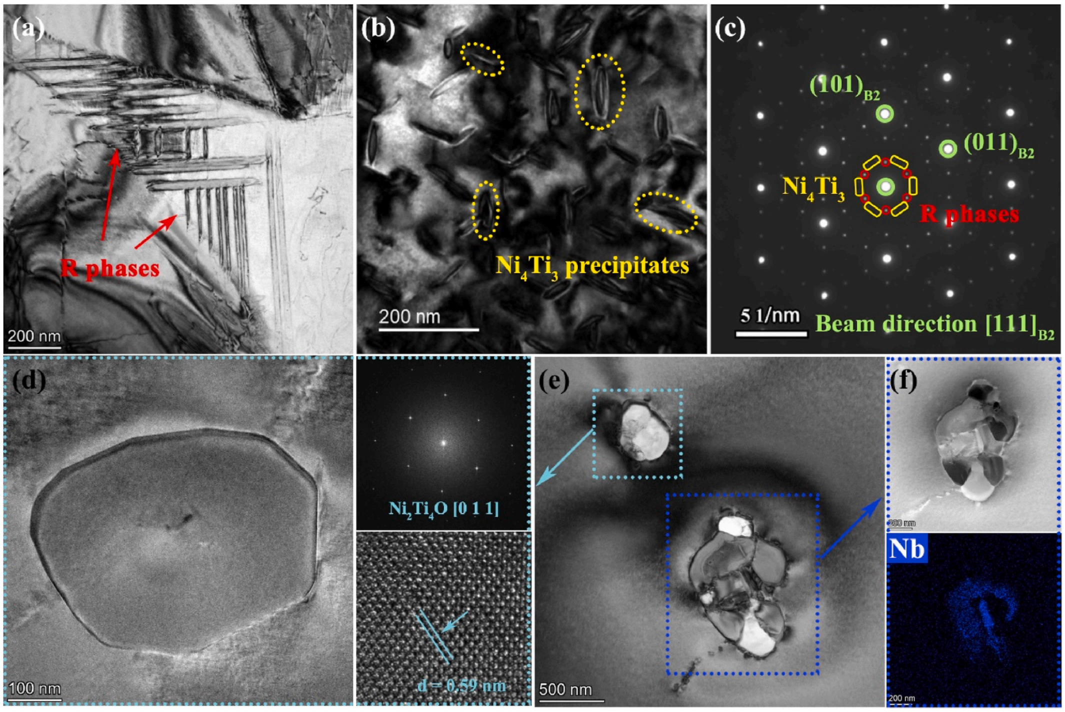

Fig. 2. TEM analysis of (a) bright-field images of R phases in aged S0; (b) bright-field images of needle-like Ni_4Ti_3 precipitates in aged S0; (c) corresponding SAED pattern in (b). (d) HRTEM images of precipitates in aged S3 and corresponding FFT image in (e); (e) bright-field images of aged S3; (f) EDS mapping of selected area in (f).

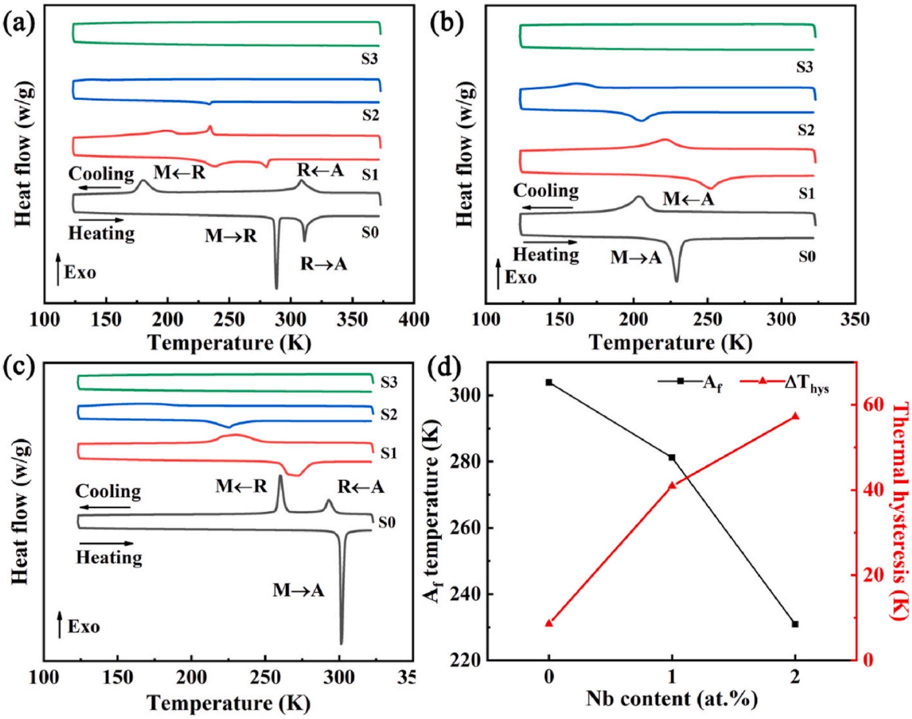

Fig. 3. DSC curves of $NiTiNb_x$ ($x = 0, 1, 2, 3$) alloys in (a) as-cast, (b) solution-treated, and (c) aged state; and the dependence of A_f temperature and thermal hysteresis ΔT_{hys} of aged samples on the Nb content.

sample exhibits a reversible two-stage B2↔R↔B19' transformation during both heating and cooling. After solution treatment, only a single B2↔B19' transformation peak remains. Aging treatment restores the two-stage transformation during cooling (B2→R→B19') while maintaining a single-stage transformation (B19'→B2) during heating. The aged S0 sample has an AT finish temperature A_f of 303.92 K, which is slightly above room temperature. With 1 at. % Nb addition (S1), the as-cast sample still shows a two-stage transformation, but the solution-treated and aged samples display only a single-stage transformation. Compared to aged S0, both the MT and AT temperatures are decreased significantly in aged S1, with the A_f temperature dropping to 281.16 K, which is below room temperature. Further, the thermal hysteresis ΔT_{hys} is enlarged to 40.94 K, while the transformation enthalpy for the thermal-induced MT and AT decreases. For the S2 alloy, single-stage transformation is observed in all conditions, with A_f further decreasing to 231.08 K. The S3 alloy shows no detectable peaks, indicating complete suppression of thermal-induced MT. The influence of Nb content on A_f and ΔT_{hys} is summarized in Fig. 3 (d). Increasing Nb content progressively decreases A_f while increasing ΔT_{hys}. The phase transformation temperature and corresponding enthalpy change of thermal-induced phase transformation in the four aged samples are summarized in Table 2.

The two-stage transformation behavior in binary NiTi alloys originates from Ni_4Ti_3 precipitates, which generate localized stress fields that inhibit direct B2↔B19' transformation and promote the intermediate R-phase transformation [42]. During rapid solidification, various intermetallic phases, including Ni_4Ti_3 precipitate from the matrix, result in the characteristic two-stage transformation observed in the as-cast NiTi samples. Subsequent solution treatment effectively dissolves these precipitates, thereby eliminating the R-phase transformation pathway. However, aging treatment facilitates the reprecipitation of Ni_4Ti_3, restoring the two-stage transformation behavior. In Nb-doped alloys, as no Ni_4Ti_3 precipitation during solution and aging treatment, only a single-stage B2–B19' phase transformation happens.

The incorporation of Nb produces three distinct effects on the transformation characteristics for aging samples: (1) a significant reduction in phase transformation temperatures, (2) a decrease in transformation enthalpies, and (3) a notable increase in thermal hysteresis. The A_f is particularly critical for shape memory alloys intended for solid-state refrigeration applications, as both superelasticity and the elastocaloric effect are only manifested above this temperature. Thus, A_f effectively defines the lower operational limit for these functional properties. The reduction of transformation temperatures in Nb-doped alloys can be attributed to two primary factors. First, the substitution of Nb alters the effective Ni/Ti ratio in the matrix, which is known to significantly influence the transformation behavior in near-equiatomic NiTi alloys [44]. Second, the dissolved Nb atoms induce lattice distortions and create localized stress fields that thermodynamically stabilize the parent phase [24]. As the Nb concentration increases, the matrix becomes progressively more disordered with enhanced local strain fields, while the martensitic phase develops increasing structural imperfections.

When the Nb content exceeds 3 at. %, the thermal-induced MT is completely suppressed, possibly replaced by a short-order strain glass transition. This strain glass state is not unique to NiTiNb systems, as analogous effects have been reported in other ternary NiTi*X* alloys ($X =$ Co, Cr, Mn) [22,24,45]. The Nb doping effectively reduces the thermodynamic driving force for martensitic transformation, as evidenced by the progressive decrease in phase transformation temperature. Consequently, the associated enthalpy changes (e.g., $\Delta H_{A\rightarrow M}$) diminish due to reduced strain ordering during transformation. While extensive research has documented the exceptionally wide thermal hysteresis (ΔT_{hys}) in eutectic $Ni_{47}Ti_{44}Nb_9$ alloys, where β-Nb precipitates are considered primarily responsible for transformation inhibition and hysteresis enhancement [31,46,47], the current study on low-Nb micro-alloying NiTiNb demonstrates that the dissolved Nb atoms play the dominant role in increasing kinetic resistance to MT. This conclusion is supported by recent investigations and is particularly evident in alloys containing minimal β-Nb phase formation [36,48,49]. The results underscore the importance of solute effects in governing the transformation characteristics of micro-alloying NiTiNb systems.

3.3. *Mechanical properties and superelastic performance*

The mechanical properties of the aged $NiTiNb_x$ samples were measured under room temperature (RT), as shown in Fig. 4 (a). A low strain rate of $10^{-4}\ s^{-1}$ was employed to maintain isothermal conditions during testing. To ensure measurement accuracy, all strain curves were baseline-corrected by subtracting the results obtained without specimens to eliminate fixture displacement effects. Compression curves revealed distinct transformation plateaus in all $NiTiNb_x$ samples (Fig. 4 (a)), with the underlying mechanism (stress-induced martensitic transformation or stress-induced martensitic reorientation) dependent on test temperature relative to A_f. For the S1–S3 samples tested at RT, above A_f of each sample, the stress plateau resulted exclusively from the stress-induced MT. Differently, the coexistence of austenite and martensite observed in S0 at RT (between A_s and A_f) indicates that the stress plateaus originate from simultaneous stress-induced MT and martensite reorientation. The complete stress-strain response can be divided into four characteristic stages: initial elastic deformation of austenite; stress-induced MT initiation at the critical stress (σ_{MS}) producing the transformation plateau; elastic deformation of martensite with partial plasticity following transformation completion; and finally, plastic deformation of the martensite leading to fracture failure. It is shown that the σ_{MS} increases progressively with Nb addition (S1–S3), indicating enhanced mechanical stability of the parent B2 phase at the test temperature. However, the martensite yield strength (σ_y) displayed an opposite trend, suggesting Nb-induced softening of the martensitic phase. The transformation plateau length was also extended with increasing Nb content. While the S0–S2 samples showed comparable fracture strength (σ_f) and ductility (ε_f), the S3 composition demonstrated improved performance in both mechanical properties. These results collectively demonstrate that Nb addition effectively strengthens the parent phase while modifying the martensite mechanical behavior.

Fig. 4(b)–(e) presents the cyclic stability of the superelastic behavior in the four alloy samples. All specimens used for cyclic testing were newly prepared and previously untested. Considering that functional properties (superelasticity and elastocaloric effect) in SMAs typically experience great degradation during the initial cycles, we conducted 10 complete loading-unloading cycles for each sample [50]. Based on the above results, we applied different strain amplitudes (approximately 4.5 % for S0 and 6 % for S1–S3) to ensure a full superelastic response. By the tangent method, we determined the critical transformation stress (σ_{MS}) and transformation strains starting points and finishing points (ε_{MS} and ε_{MF}), with the transformation strain (ε_{MT}) calculated as their difference. The mechanical test results of four samples at near RT are tabulated in Table 3. As demonstrated in Fig. 4 (b), the aged S0 sample exhibited a 50.84 % strain recovery rate during the first cycle at 316 K (slightly above its A_f temperature from DSC measurements), with an applied strain of 4.69 %. The residual strain (ε_{ir}) progressively decreased with cycling, approaching zero by the 10th cycle. While the σ_{MS} remained relatively constant throughout cycling, the ε_{MT} gradually decreased with an increasing number of cycles. Notably, the Nb-containing samples (Fig. 4(c)–(e)) showed significantly lower

Table 2

Phase transformation temperatures, thermal hysteresis, and transformation enthalpy change of aged NiTiNb*x* ($x = 0, 1, 2, 3$) alloys.

Nb content (at. %)	M_s/R_s (K)	M_f/R_f (K)	M_p/R_p (K)	A_s (K)	A_f (K)	A_p (K)	ΔT_{hys} (K)	$\Delta H_{A\rightarrow M}$ (J g^{-1})	$\Delta H_{M\rightarrow A}$ (J g^{-1})
0	297.51	289.45	292.88	299.94	303.92	301.45	8.58	12.54	17.08
1	249.28	214.02	231.63	261.90	281.16	272.70	40.94	11.78	14.16
2	190.96	–	169.49	211.84	231.08	226.29	57.20	5.03	6.62
3	–	–	–	–	–	–	–	–	–

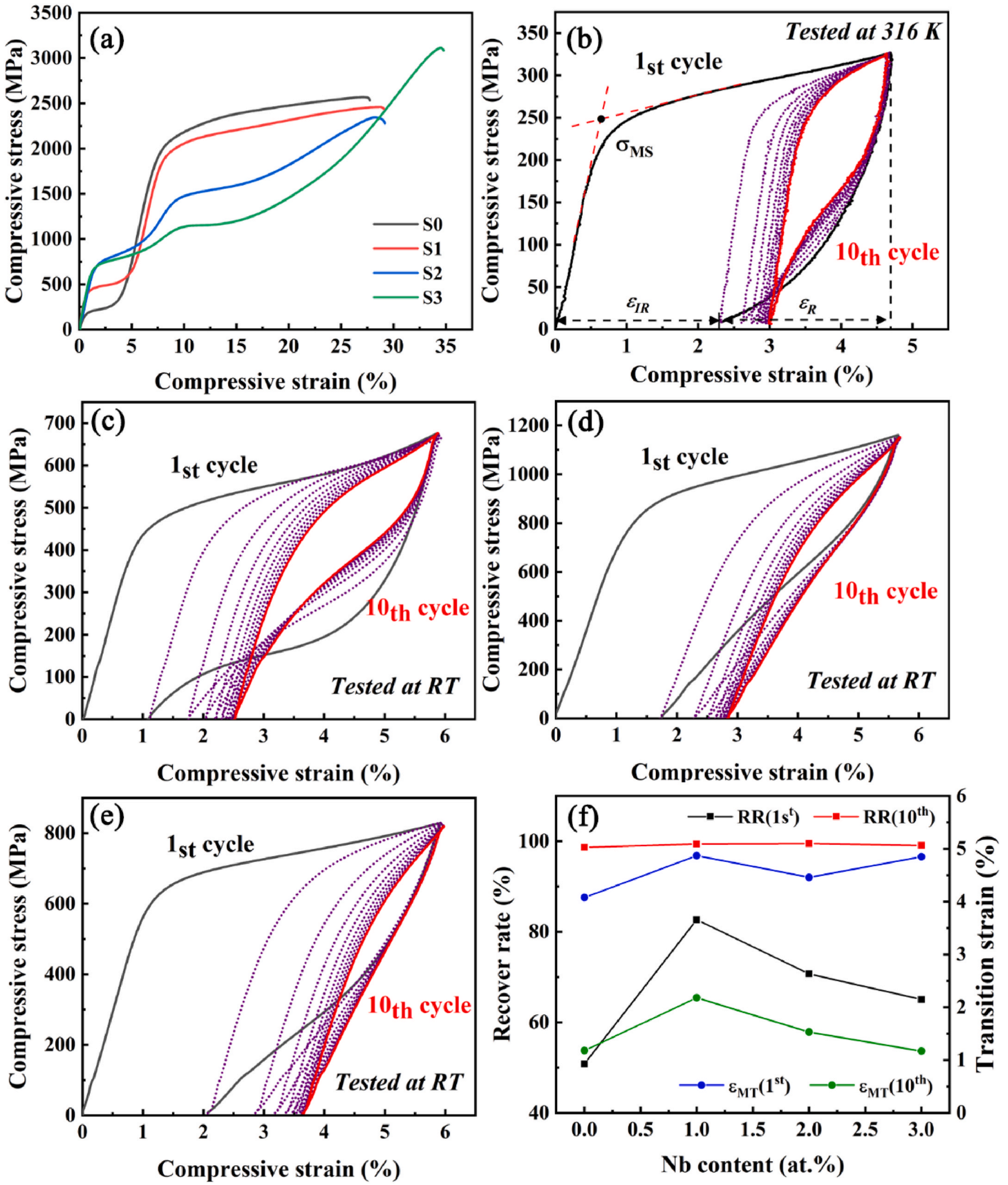

Fig. 4. (a) Compressive fracture stress-strain curves of aged NiTiNbx ($x = 0, 1, 2, 3$) alloys (316 K for the aged NiTi sample and RT for the aged S1, S2 and S3 samples); Isothermal superelasic response recorded 10 cycles of loading and unloading for the aged (b) S0 (tested at 316 K), (c) S1 (tested at RT), (d) S2 (tested at RT), (e) S3 (tested at RT) with a low loading and unloading rate at 10^{-4} s^{-1}; (f) The dependence of recovery rate (RR) and martensite transition strain on the Nb content.

Table 3
Summary of the mechanical response of aged NiTiNbx (x = 0, 1, 2, 3) alloys.

	σ_f (MPa)	ε_f (%)	σ_{MS} (MPa)	ε_{MT} (1st cycle) (%)	ε_{MT} (10th cycle) (%)	Recovery rate (1st cycle) (%)	Recovery rate (10th cycle) (%)	σ_h (10th cycle) (MPa)
NiTi	2564.22	27.46	248.41	4.08	1.18	50.84	98.66	165.89
$NiTiNb_1$	2458.22	28.62	488.96	4.87	2.18	82.66	99.42	170.84
$NiTiNb_2$	2344.85	28.18	889.11	4.46	1.53	70.71	99.5	203.81
$NiTiNb_3$	3114.15	34.49	663.67	4.85	1.17	65.07	99.08	148.73

first-cycle ε_{ir} values compared to S0, demonstrating enhanced near RT superelasticity with minor Nb additions. Particularly, the S1 alloy achieved exceptional recovery rates of 82.66 % in the first cycle and 99.42 % by the 10th cycle under 5.9 % applied strain at room temperature, as shown in Fig. 4 (c). In addition, the aged S2 sample exhibited the highest σ_{MS} (889.11 MPa) coupled with substantial ε_{MT} (4.46 %). All samples reached near-complete recoverability after 10 cycles, with the transformation parameters stabilizing after 5 cycles, as evidenced by minimal changes in both the transformation strain and stress hysteresis.

The MT transformation strain (ε_{MT}) serves as a crucial parameter for both superelasticity and elastocaloric effects in SMAs, with larger ε_{MT} values enabling greater recoverable strain. Table 3 presents the specific ε_{MT} values obtained during cyclic stability tests near RT for all four samples. As shown in Fig. 4(b)–(e), the transformation strain undergoes significant degradation during the initial cycles due to substantial irrecoverable strain accumulation, but stabilizes after approximately 6 cycles. Stress hysteresis arises from frictional dissipation during MT and quantifies energy losses per mechanical cycle [51]. Minimizing hysteresis is therefore critical for achieving high energy conversion efficiency in elastocaloric applications [52]. In this study, stress hysteresis was determined as the stress difference between the loading and unloading paths at half-transformation strain. The stress hysteresis was considerably larger in the first cycle compared to the tenth cycle for all samples, as summarized in Table 3. Although the stress-strain loops appear more linear with increasing Nb content, the applied stress was notably higher for the S1–S3 samples compared to S0. The recovery rate initially increased, then decreased with rising Nb content in the first cycle, while all samples achieved approximately 99 % recovery after 10 cycles. The transition strain of Nb-doped samples was significantly improved compared to the Nb-free S0 in the first cycle, though all samples showed substantial deterioration after 10 cycles. Among them, S1 and S2 maintained higher ε_{MT} values than S0, while S3 exhibited the poorest performance. These results demonstrate that a minor Nb addition enhances superelasticity and cyclic stability at RT, while excessive doping produces adverse effects. The complete mechanical responses, including fracture and cyclic stability data, are summarized in Table 3. The optimal composition (S1) achieved an 82.66 % recovery rate in the first cycle (compared to 50.84 % for S0) and a 99.42 % recovery rate by the tenth cycle, along with excellent transition strain.

Fig. 5 presents the temperature-dependent superelastic response of $NiTiNb_x$ alloys, showing the 10th cycle stress-strain curves for better comparison of superelastic performance across different temperatures.

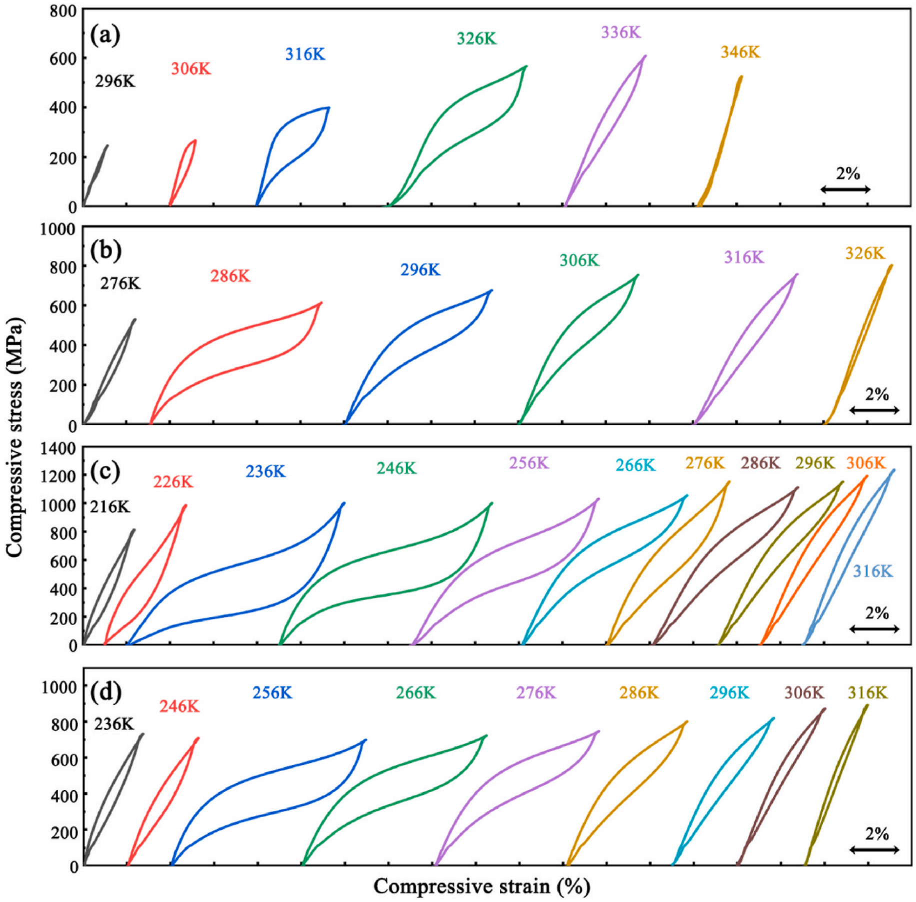

Fig. 5. Isothermal compressive stress-strain curves measured with a low strain rate of 10^{-4} s^{-1} for (a) S0; (b) S1, (c) S2, and (d) S3 at different temperatures.

The binary S0 alloy displays purely linear elastic behavior at both 296 K and 346 K after 10 cycles (Fig. 5 (a)), indicating complete loss of superelasticity and establishing a working temperature window of approximately 30 K. The S1 alloy demonstrates clear superelasticity between 286 and 316 K, with nearly linear but still slightly superelastic responses at the boundary temperatures (276 K and 326 K), as shown in Fig. 5 (b). While both S0 and S1 exhibit comparable 40 K operational ranges, S1 shows superior superelastic performance at intermediate temperatures compared to the limited recoverable strain of S0. Furthermore, the working temperature window of the S1 alloy exhibits a distinct downward shift compared to the binary S0 alloy, demonstrating excellent agreement with the reduced AT finish temperature (A_f = 281.16 K) observed in the DSC thermograms (Fig. 3). This correlation confirms that the Nb-induced depression of the transformation temperatures effectively translates to lower operational ranges for superelastic applications. The 22.76 K reduction in A_f (from 303.92 K in S0 to 281.16 K in S1) corresponds well with the observed 20–30 K downward shift in the optimal superelastic performance window. Increasing the Nb content to 2 at.% (S2, Fig. 5 (c)) significantly expands the working temperature window beyond 100 K, with optimal superelastic behavior occurring at remarkably lower temperatures (236–246 K) compared to the best superelasticity of S0 at 326 K. However, further Nb addition to 3 at.% (S3, Fig. 5 (d)) reduces the operational window to 90 K while shifting the optimal superelastic temperature to 256 K. It should be noted that different applied strain levels were used (approximately 4.5 % for S0 versus 6 % for S1–S3) to accommodate the transformation characteristics of each alloy. These results demonstrate a non-monotonic relationship between Nb content and functional performance: the working temperature window initially expands with increasing Nb content up to 2 at.% before contracting at higher concentrations, while the temperature for optimal superelasticity follows an inverse trend, first decreasing then increasing with Nb addition.

Fig. 6 (a) illustrates the temperature dependence of the critical stress for stress-induced martensitic transformation (σ_{MS}), measured during the first cycle of compressive testing. The σ_{MS} values for all four samples exhibit a characteristic linear increase with temperature. Linear fitting of these data yields a stress-temperature coefficient of ~8.31 MPa/K for the S0 alloy, which agrees well with previously reported values for NiTi alloys [53]. With the addition of Nb, this coefficient systematically decreases, as clearly shown by the $d\sigma/dT$ versus Nb content plot in Fig. 6 (b). Fig. 6 (c) presents the dependence of isothermal entropy change of the NiTiNb$_x$ associated with the stress-induced MT on the testing temperature, calculated from the loading curves in the 1st cycle during the compressive cyclic tests using the Maxwell relation: $(\partial\sigma/\partial T)_\varepsilon = (\partial S/\partial\varepsilon)_T$

$$\Delta S_{iso} = \int_0^\varepsilon \left(\frac{\partial\sigma}{\partial T}\right)_\varepsilon d\varepsilon \tag{1}$$

Table 4 summarizes the calculated ΔS_{iso} values along with the peak temperature (PT) and working temperature window (defined by the illustration in Fig. 6 (c)). Fig. 6 (d) shows the variation of both the

Table 4
Theoretical isothermal entropy change, temperature at peak, and working temperature window from entropy change-temperature curves calculated using the Maxwell relation.

Nb content (at. %)	Maximum ΔS_{iso} (J/kg•K)	Working temperature window (K)	Temperature at peak (K)
0	67.72	26.76	324.97
1	48.81	66.21	283.91
2	46.98	118.84	238.37
3	31.37	90.87	268.25

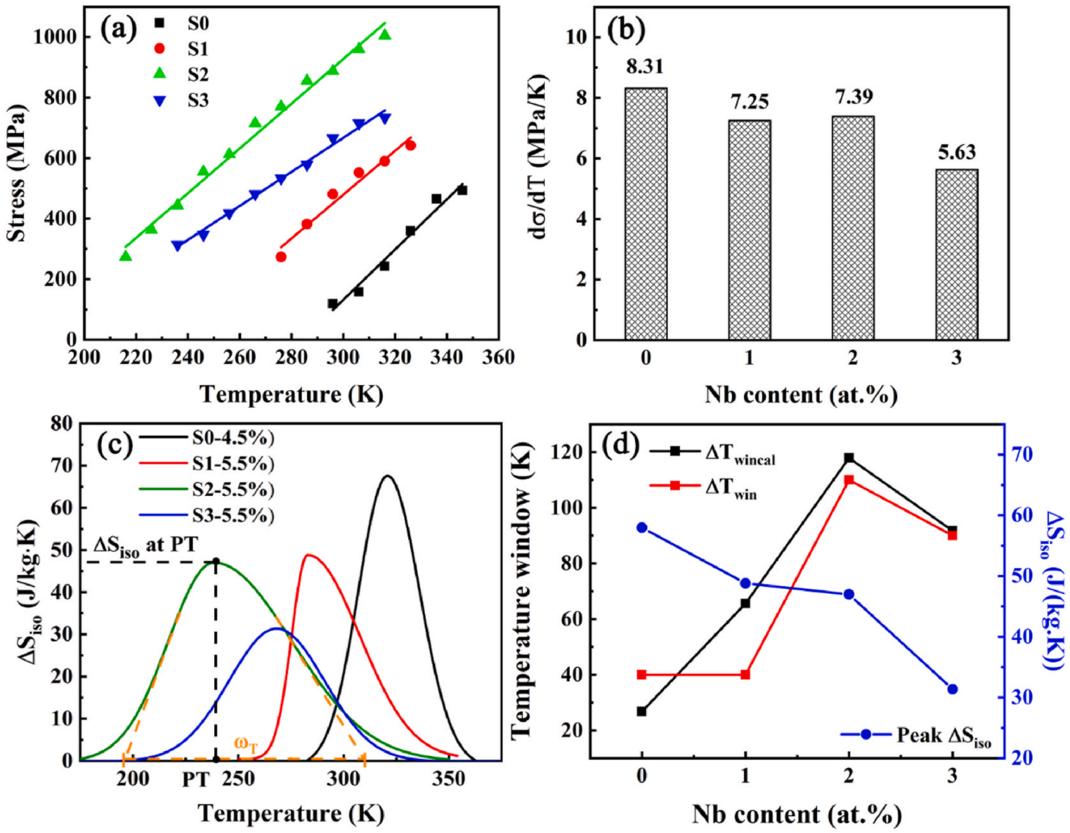

Fig. 6. (a) The dependence of the critical stress for martensite transformation on temperature. The solid lines are the results of linear fitting. (b) The dependence of dσ/dT on Nb content, which is the slope of the linear fitting line in (a). (c) The temperature dependence of entropy changes ΔS_{iso} calculated from the strain-temperature relation using the Maxwell relation. (d) The dependence of the working temperature window and entropy changes ΔS_{iso} on Nb content.

working temperature window and ΔS_{iso} with Nb content. The ΔS_{iso} decreases progressively with increasing Nb content, while the working temperature window initially expands before contracting at higher Nb concentrations. Notably, the S2 alloy achieves a theoretical working temperature window of 118.84 K, approximately triple that of the S0 sample. This trend in the working temperature window and the opposite behavior of PT with Nb content are fully consistent with the experimental results from the temperature-dependent cyclic tests.

To evaluate the optimal superelastic performance of each alloy composition, we conducted compressive cyclic stability tests at their respective peak temperatures (PT), as determined from the above results, with the data presented in Fig. 7. Table 5 summarizes the key parameters, including recovery rate, martensitic transformation strain (ε_{MT}), and stress hysteresis for both the first and tenth cycles. To ensure complete stress-induced martensitic transformation at each sample's PT, we applied different strain levels: approximately 4.5 % for S0, 6 % for S1, 6.5 % for S2, and S3. Comparative analysis reveals significant improvements in superelastic performance at PT relative to RT testing conditions. All samples demonstrated enhanced recovery rates in both initial and stabilized (10th) cycles when tested at their PT. Notably, the S2 exhibited exceptional performance with a 97.18 % recovery rate during the first cycle at 238 K, the highest among all tested samples. It is shown that testing at PT yields several improvements: (1) prolonged ε_{MT} values, (2) increased stress hysteresis, and (3) superior cyclic stability compared to performances at RT. Among the four samples, the S2 exhibits the highest recovery rate and functional stability. These results clearly demonstrate that testing at material-specific optimal temperatures substantially enhances both the superelastic response and cyclic stability compared to conventional RT evaluation. The performance hierarchy based on the working temperature window (S2 > S1 > S3 > S0) provides valuable guidance for alloy selection in applications requiring superelastic performance in a wider temperature range.

Table 5
The superelastic response of aged NiTiNb$_x$ alloys at the PT.

Nb content (at. %)	Recovery rate (1st cycle) (%)	Recovery rate (10th cycle) (%)	ε_{MT} (1st cycle) (%)	ε_{MT} (10th cycle) (%)	σ_h (1st cycle) (MPa)	σ_h (10th cycle) (MPa)
0	85.48	99.63	3.97	1.99	334.25	158.66
1	88.22	99.34	5.19	3.04	415.14	177.96
2	97.18	99.14	5.28	4.02	387.07	299.55
3	88.65	99.02	5.62	3.23	439.21	191.82

We first evaluated the superelastic performance of all four samples under near-RT conditions, with the results presented in Fig. 4 and Table 3. The analysis revealed that while the S1 alloy demonstrated an impressive initial recovery rate of 82.66 %, all samples exhibited varying degrees of residual strain, indicating the temperature-sensitive nature of superelastic behavior in these materials. The superelastic response shows a strong dependence on the testing temperature that follows several fundamental principles. First, the superelastic effect only exists when the testing temperature exceeds the AT start temperature (A_s), at which the austenite phase starts existing in the matrix. As the temperature increases from the A_s to A_f, the superelastic performance improves progressively due to the increasing fraction of austenite phase available for MT [54]. However, this improvement reaches an optimum point as the testing temperature continues to rise above A_f, where two competing factors come into play. On the one hand, the critical stress for stress-induced MT increases with temperature, while on the other hand, the yield strength of the matrix decreases [55]. Consequently, the matrix

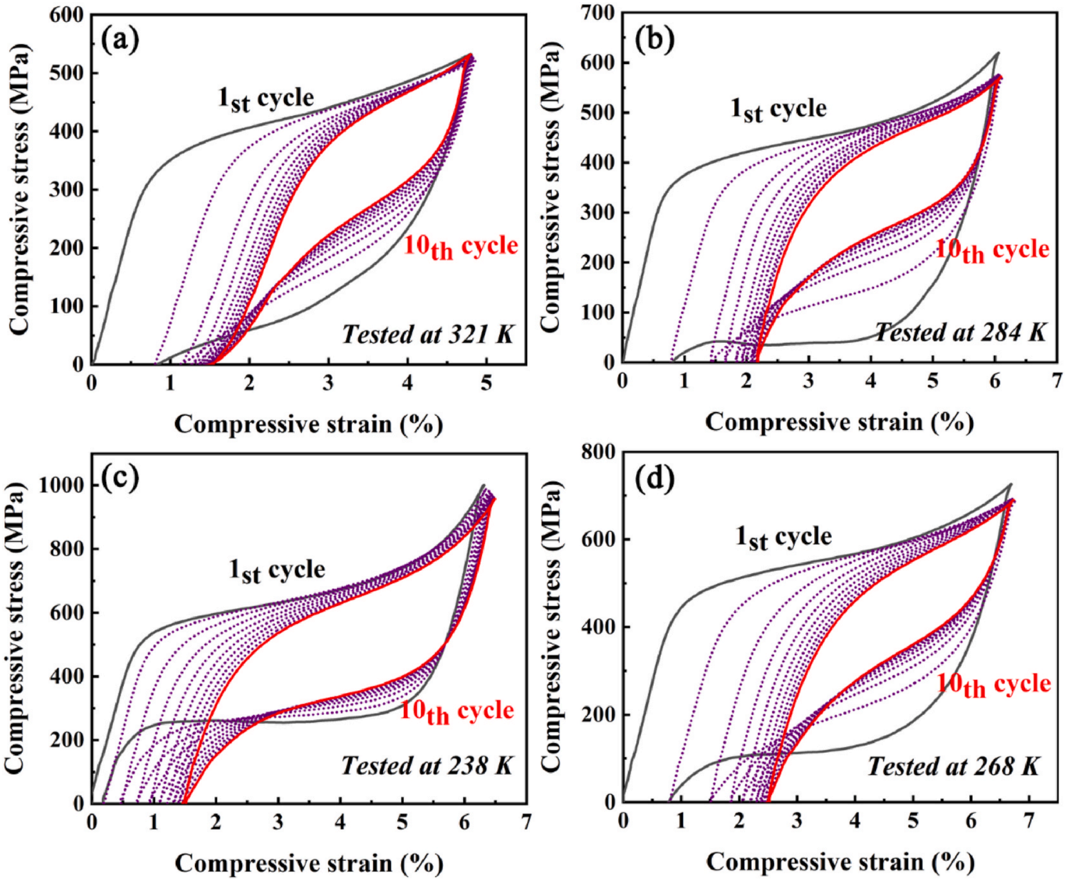

Fig. 7. Isothermal superelasic response recorded for 10 cycles of loading and unloading for the aged samples (a) S0 (tested at 321 K), (b) S1 (tested at 284 K), (c) S2 (tested at 238 K), (d) S3 (tested at 268 K) with a low loading and unloading rate at 10^{-4} s^{-1}.

increasingly undergoes plastic deformation rather than stress-induced MT, leading to progressive degradation of the superelastic performance. This fundamental competition between MT and dislocation slips gives rise to a characteristic temperature dependence of superelastic properties: the performance initially improves with increasing temperature as the austenite phase fraction grows, and reaches an optimum when the thermodynamic driving force for transformation is balanced against the resistance to plastic yielding, and subsequently declines until superelasticity is completely suppressed. As demonstrated in Fig. 5, this non-monotonic temperature dependence follows a characteristic bell-shaped curve that aligns with the Gaussian-like distribution predicted by Maxwell relation analysis in Fig. 6 (c), confirming the thermodynamic consistency between experimental observations and theoretical calculations. DSC measurements presented in Fig. 3 show that the AT finish temperature (A_f) decreases systematically with increasing Nb content in these alloys. This compositional dependence means that while the absolute testing temperatures were maintained at similar levels (316 K for S0 and room temperature for S1–S3), their relative positions with respect to each alloy's specific A_f varied significantly. The S1 alloy, with the smallest temperature difference between its A_f (281.16 K) and RT, consequently demonstrated superior room-temperature superelastic performance compared to the other compositions in this study.

To enable a more comprehensive comparison of superelastic performance for the four alloys, we conducted additional compressive cyclic tests at the individual PT of each sample, determined from the Maxwell relation analysis. These tests, whose results are shown in Fig. 7 and summarized in Table 5, confirmed that all compositions exhibited enhanced superelastic performance at their respective PT compared to RT testing. Particularly noteworthy was the performance of the S2 alloy, which achieved an exceptional 97.18 % recovery in the first cycle at 238 K under 5.28 % applied strain, despite the samples receiving no prior training or mechanical pre-deformation treatment. The experimental results also revealed that all samples displayed some degree of irrecoverable strain, even when tested at their optimal temperatures. This phenomenon, commonly observed in NiTi-based shape memory alloys, originates from the plastic deformation occurring in the partial matrix during mechanical cycling. The dislocations generated during repeated loading-unloading cycles create localized strain fields that can stabilize certain martensitic variants, preventing their complete transformation back to austenite upon unloading. However, as cycling continues, the dislocation density eventually reaches saturation, resulting in progressively smaller increments of irrecoverable strain with each subsequent cycle [34]. Furthermore, these accumulated dislocations and stabilized martensitic variants can generate beneficial internal stress fields that gradually reduce energy dissipation during cycling, as evidenced by the decreasing stress hysteresis observed in the above results (Fig. 7 and Table 5).

The working temperature window represents a crucial performance parameter for superelastic and elastocaloric materials, as it fundamentally determines the operational temperature range where the SMAs can function effectively as a solid-state refrigerant. Since both superelasticity and elastocaloric effects originate from stress-induced MT, their working temperature windows are intrinsically linked. In this study, we characterized the working temperature window through temperature-dependent superelasticity measurements for each alloy composition. Referring to Figs. 5 and 6 (c), the working temperature window exhibits a non-monotonic dependence on Nb content, initially expanding before contracting with increasing Nb concentration. This behavior can be understood through two primary mechanisms governing the window's boundaries: At the lower temperature limit, the phase transformation temperature plays a decisive role. Nb substitution for Ni modifies the matrix composition, altering the Ni/Ti ratio and consequently depressing A_f. Additionally, dissolved Nb atoms act as point defects that both reduce the thermodynamic driving force for long-range martensitic ordering and create localized stress fields that stabilize the austenitic matrix [24]. These combined effects produce the observed downward shift in transformation temperatures with increasing Nb content. The upper temperature limit is primarily governed by yield strength. Previous studies have demonstrated that proper Nb additions (1–2 at.%) enhance yield strength through synergistic solid solution and precipitation strengthening mechanisms [35]. This strengthening effect becomes particularly relevant when considering the fundamental relationship describing the working temperature window [56,57]: $\Delta T_{win} = \sigma_y/(d\sigma/dT) - \Delta T_{hys}$. where σ_y is the yield strength, $d\sigma/dT$ represents the temperature sensitivity of the transformation stress, and ΔT_{hys} denotes the thermal hysteresis. Although direct measurement of σ_y is precluded by prior stress-induced MT, this relationship reveals that both increased σ_y and reduced $d\sigma/dT$ (as observed in Fig. 6 (b)) contribute to temperature window expansion by maintaining the stress threshold for stress-induced MT over a wider temperature range before plastic deformation starts. However, excessive Nb addition (3 at.%) proves detrimental to temperature window, as the associated increasing of 'point defects' and precipitates creates excessive local stress fields that over-stabilize the austenite, leading to a increases of critical stress for stress-induced MT. Similar phenomenon also happens in Fe-doped NiTi SMAs and NiTiCuFe SMAs [23,58]. As a result, the matrix starts plastic deformation instead of stress-induced MT as the critical stress for MT is beyond the yield strength. In addition, the vanishing of superelasticity at lower temperatures is probably resulting from the increase in phase transformation temperature. These two factors explain the subsequent window contraction with higher Nb addition. The theoretically calculated working temperature windows derived from Maxwell relations (Fig. 6 (d)) show excellent agreement with experimental observations, with the S2 alloy achieving the optimal performance, demonstrating a threefold enhancement (100 K experimentally, 118.84 K theoretically) compared to S0. These results establish clear composition-property relationships for designing NiTiNb alloys with tailored working temperature windows.

3.4. Elastocaloric effect

The elastocaloric effect of aged NiTiNb$_x$ alloys was investigated through temperature monitoring during stress loading and unloading cycles. Following the strain levels established in prior cyclic stability tests (4.5 % for S0, 6 % for S1–S3), we performed 10 cycles under near-adiabatic conditions via a high strain rate 10^{-1} s^{-1} at temperatures above A_f (RT for S1–S3, 316 K for S0) as shown in Fig. 8. Each test cycle consisted of rapid loading to maximum strain followed by a 15 s recovery period for equilibrating to test temperature, subsequent unloading to 50 MPa stress, and finally a 30 s holding period before initiating the next cycle. As seen from the dependence of temperature on time profiles in Fig. 8(a)–(d), the four aged NiTiNb$_x$ samples all exhibit a large elastocaloric effect during the loading and unloading process at near RT. The adiabatic temperature change during the loading and unloading process in the 1st and 10th cycles is tabulated in Table 6. As the elasotocaloric application is mainly related to the heat absorption, we mainly focus on the adiabatic temperature change ΔT_{ad} during the unloading process in this work. As shown in Fig. 8(a)–(d), all alloys exhibited significant temperature variations during transformation, with the aged S1 sample demonstrating particularly remarkable performance. The first-cycle ΔT_{ad} during the unloading process reached −12.3 K for S1, surpassing the −9.13 K observed for S0. However, all samples showed substantial degradation in ΔT_{ad} by the 10th cycle, with values decreasing to −7.44 K (S0), −8.37 K (S1), −3.76 K (S2), and −3.01 K (S3). This degradation was most pronounced during the initial 5 cycles before stabilizing from the 6th cycle onward, as quantified by the functional stability ratios presented in Table 6. Notably, three of the four alloys (S0, S2, and S3) exhibited asymmetric responses with larger temperature changes during loading compared to unloading, probably due to the accumulated irrecoverable strain. The exceptional

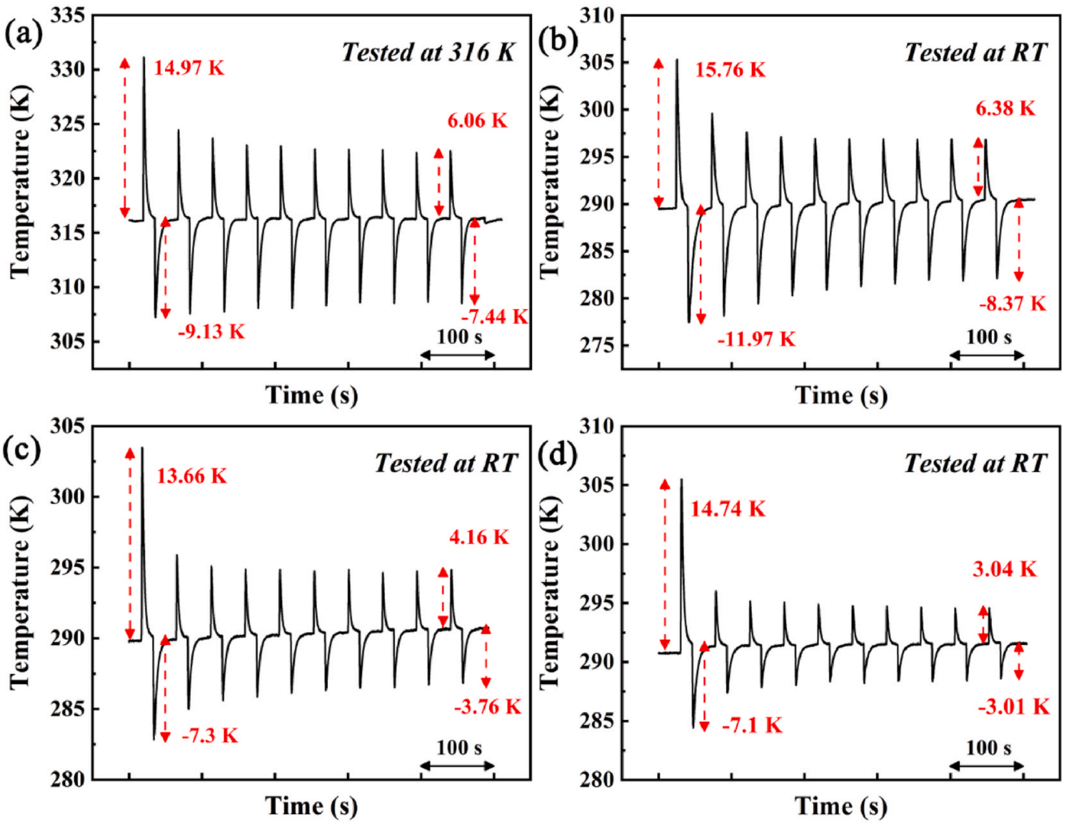

Fig. 8. The adiabatic temperature change ΔT_{ad} recorded during 10 cycles of loading and unloading for the aged samples (a) S0 (tested at 316 K), (b) S1 (tested at RT), (c) S2 (tested at RT), (d) S3 (tested at RT) with a high loading and unloading rate at 10^{-1} s^{-1} at near RT.

Table 6
Elastocaloric effect ΔT_{ad} of aged NiTiNb$_x$ alloys at RT and PT.

	Nb content (at. %)	ΔT_{ad} at RT (1st cycle) (K)	ΔT_{ad} at RT (10th cycle) (K)	Ratio of 1st and 10th at RT (%)	ΔT_{ad} at PT (1st cycle) (K)	ΔT_{ad} at PT (10th cycle) (K)	Ratio of 1st and 10th at PT (10th cycle) (%)
Loading	0	14.97	6.06	40.48	13.11	6.21	47.37
	1	15.76	6.38	40.48	16.52	8.49	51.39
	2	13.66	4.16	30.45	14.57	7.26	49.83
	3	14.74	3.04	20.62	12.48	5.85	46.88
Unloading	0	−9.13	−7.44	81.49	−10.18	−7.62	74.85
	1	−11.97	−8.37	68.05	−12.02	−9.16	78.49
	2	−7.3	−3.76	51.51	−10.07	−6.09	59.82
	3	−7.1	−3.01	42.39	−9.2	−6.19	67.28

performance of S1, which achieved both the highest initial and retained ΔT_{ad} after cycling, demonstrates that optimized Nb microalloying (1 at. %) can significantly enhance the elastocaloric response of NiTi-based systems under practical operating conditions while maintaining good functional stability. These results confirm that proper compositional tuning enables large elastocaloric effects at RT in Nb-microalloying NiTi alloys.

Fig. 9 presents the time-dependent temperature evolution during the first loading-unloading cycle for S1–S3 samples under varying applied strains at RT, recorded by an IR camera (left panels (a1)-(c1)). The time axis represents relative rather than absolute values, meaning the endothermic and exothermic processes did not occur simultaneously. These infrared (IR) camera measurements (80 Hz sampling rate) show discrepancies with the thermocouple data (200 Hz) presented above, probably due to the different capture frequency of the two techniques. The middle panels (Fig. 9 (a2)-(c2)) display IR images corresponding to key points (A-N) along the temperature-time curves, with a defined region R (white dashed box) and three specific measurement points (I-III, black dots) for the temperature distribution analysis. The S1 sample (Fig. 9 (a2)) exhibits a relatively uniform temperature distribution, with regions I and III showing slightly more pronounced temperature variations during transformation. In contrast, S2 (Fig. 9 (b2)) demonstrates more localized temperature changes, particularly in region II. The S3 sample (Fig. 9 (c2)) shows the most heterogeneous distribution, evident from the stark color contrast between region I (dark orange) and region III (bright green) in image D. The right panels (Fig. 9 (a3)-(c3)) quantify these temperature variations by comparing the average temperature across region R with local measurements at points I-III. While S1 maintains relatively uniform temperature evolution, S2 exhibits significant local variations, with a maximum ΔT_{ad} difference of 1.72 K between points II and III during the unloading process. Interestingly, despite the visually apparent heterogeneity in IR images of S3, its measured temperature variation (0.43 K) is actually smaller than the counterpart of S2. These results collectively demonstrate that increasing Nb content leads to progressively more localized and heterogeneous temperature distributions during elastocaloric cycling.

Fig. 10 presents the elastocaloric performance of all four samples measured at their respective PT to evaluate the maximum achievable

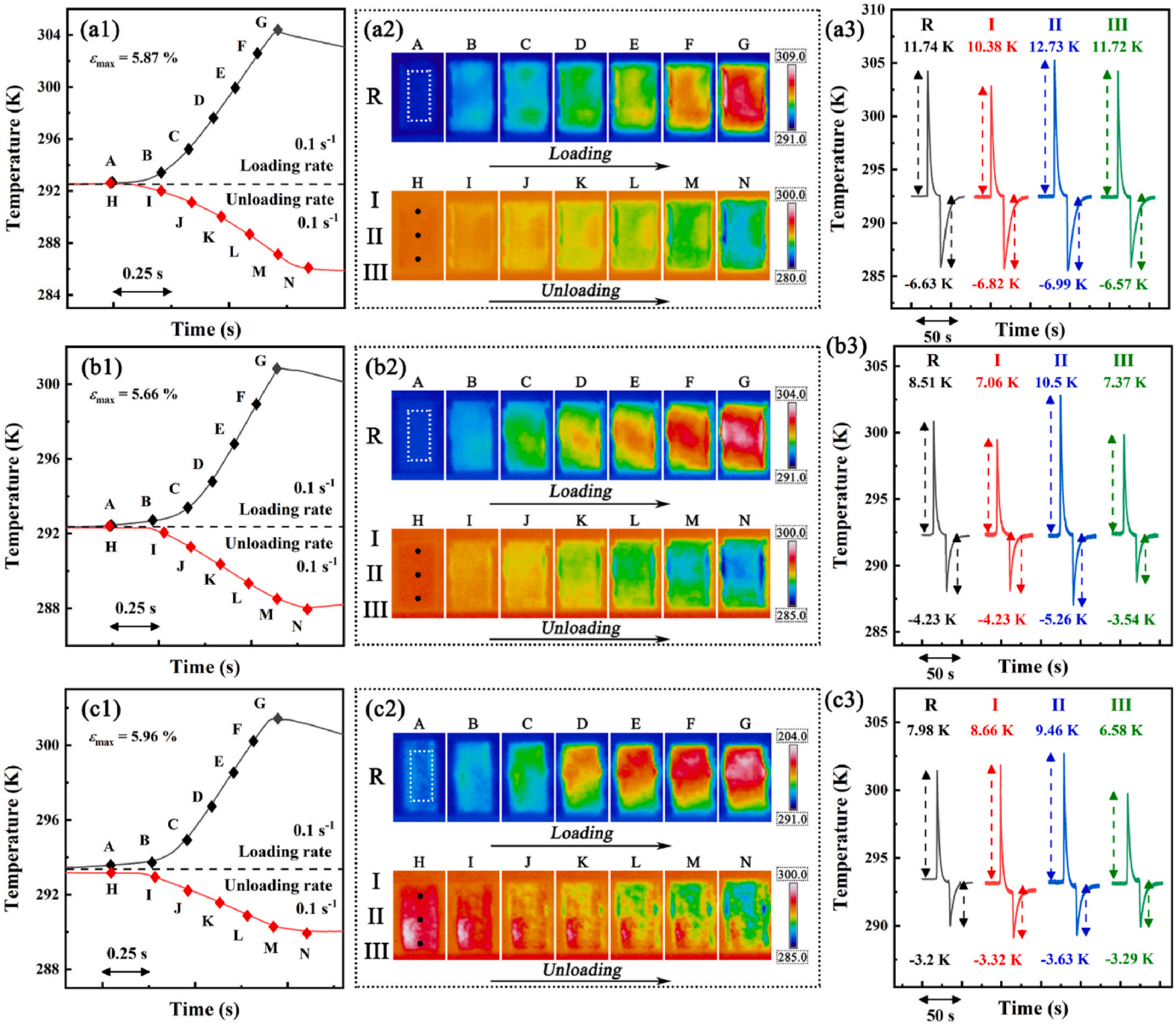

Fig. 9. The infrared thermography images and corresponding temperature-time curves of the NiTiNb$_x$ alloys during the loading, unloading, and holding processes (a1-a3) S1, (b1-b3) S2, and (c1-c3) S3.

adiabatic temperature change ΔT_{ad}. The experimental procedure followed the same protocol as the RT tests described previously. Comparative analysis reveals consistent enhancement in ΔT_{ad} values at PT compared to RT measurements for both 1st and 10th performance, as tabulated in Table 6. A notable observation concerns the reduced difference between loading and unloading ΔT_{ad} values at PT compared to RT tests. After the initial five cycles, the ΔT_{ad} values stabilize at approximately half their initial magnitude, indicating establishment of a stable functional response. The S1 composition demonstrated exceptional performance at both RT and PT conditions, achieving the highest ΔT_{ad} of -12.02 K. This consistency highlights the great elastocaloric properties of the S1 alloy throughout its operational temperature range. The temperature-dependent measurements demonstrate that while PT testing reveals the fundamental limits of each sample's elastocaloric potential, the S1 alloy maintains superior performance even under RT conditions.

The entropy change during stress-induced MT (ΔS_{iso}) represents another fundamental parameter for characterizing the elastocaloric effect. As shown in Fig. 6 (c), we initially calculated ΔS_{iso} using the Maxwell relation applied to first-cycle loading curves, with the results summarized in Table 4. For comparative analysis, we employed an alternative approach through the Clausius-Clapeyron equation to determine the entropy change (denoted as ΔS_c) [3,59]:

$$\Delta S_c = -\frac{\Delta \varepsilon_{MT}}{\rho} \cdot \frac{d\sigma}{dT} \tag{2}$$

where $\Delta \varepsilon_{MT}$ represents the transformation strain from the stress-induced martensite plateau and $d\sigma/dT$ is the temperature sensitivity of transformation stress. The mass density ρ of four samples was 6.36 ± 0.03, 6.4 ± 0.03, 6.53 ± 0.02, and 6.59 ± 0.03 g/cm^3, tested by a density balance based on Archimedes' principle. These parameters were derived from the above experimental data. The calculated ΔS_c values of 51.86, 58.75, 59.84, and 48.23 J/(kg·K) for S0, S1, S2, and S3, respectively, consistently exceeded the corresponding ΔS_{iso} values obtained via the Maxwell relation. As the numerical integration and multiple fitting procedures are employed during the evaluation based on Maxwell, the limited data of temperature-dependent stress-strain curves may generate

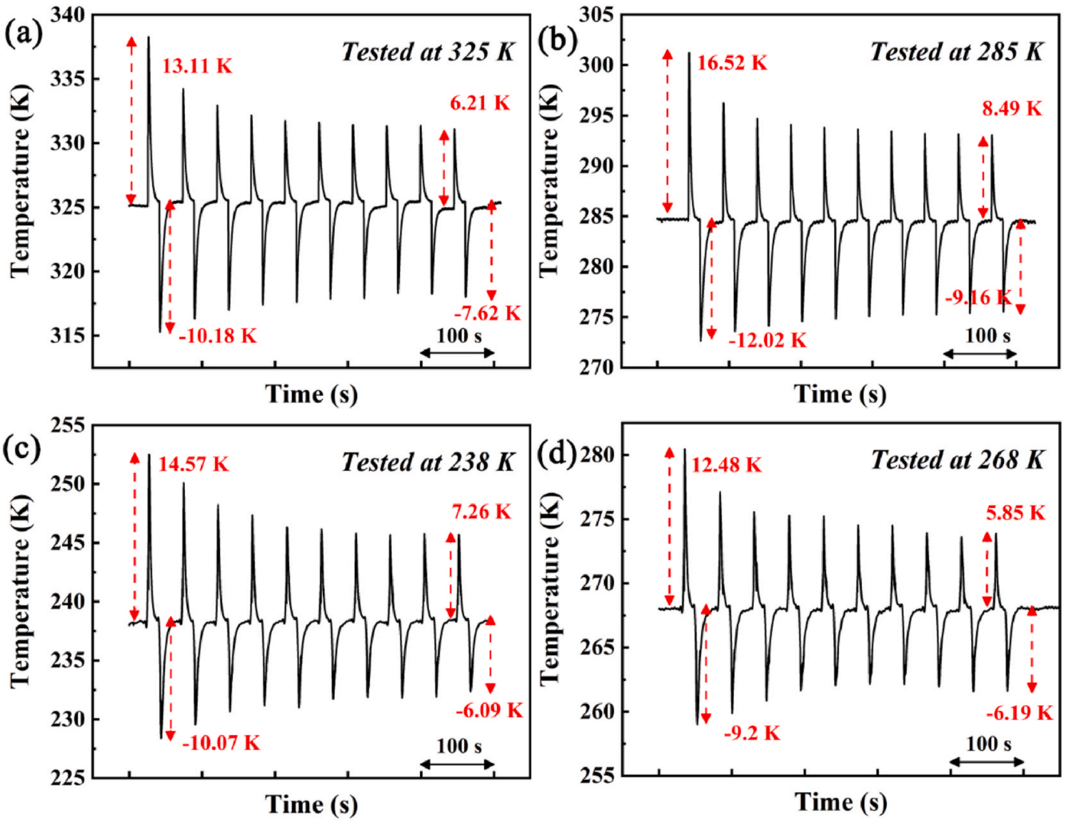

Fig. 10. The adiabatic temperature change ΔT_{ad} recorded during 10 cycles of loading and unloading for the aged samples (a) S0 (tested at 325 K), (b) S1 (tested at 285 K), (c) S2 (tested at 238 K), (d) S3 (tested at 268 K) with a high loading and unloading rate at 10^{-1} s^{-1} at PT.

more numerical errors. This suggests that the Clausius-Clapeyron method may provide a more reliable evaluation of transformation entropy changes in this work [3].

As demonstrated in Fig. 8, the NiTiNb$_x$ alloys exhibit significant elastocaloric effects during stress-induced MT at near RT conditions. The adiabatic temperature change ΔT_{ad} reaches approximately 10 K or higher in the first cycle, followed by degradation in subsequent cycles. This elastocaloric response fundamentally originates from the stress-induced MT, sharing the same physical basis as the superelastic effect observed in these materials. As discussed above, about the superelasticity, larger deviations from A_f result in reduced transformation reversibility, directly impacting both superelastic recovery rates and elastocaloric performance. The variation in performance between compositions correlates strongly with the temperature difference between the testing condition and each alloy's AT finish temperature (A_f). This relationship explains why S0 and S1, with their superior RT recovery characteristics, demonstrate more stable cyclic elastocaloric behavior compared to S2 and S3. The enhanced performance at PT conditions for all alloys further supports this explanation, as testing at the optimal transformation temperature of each sample maximizes the participating martensite volume fraction. The observed difference between loading and unloading ΔT_{ad} values in the first cycle arises from two primary reasons. First, the incomplete reverse transformation leaves residual martensite variants that cannot contribute to the temperature change during unloading. Second, energy dissipation through plastic deformation during the initial cycles generates additional heating during loading that is not recovered during unloading, as reported in many studies [41–43]. In addition, it is observed that the ΔT_{ad} degrades gradually with cycling, for instance, −12.02 K in the 1st cycle and −9.16 K in the 10th cycle of S1 alloy at PT. As both superelasticity and elastocaloric effect originate from the stress-induced MT, the reason for deterioration of ΔT_{ad} is also mainly attributed to two reasons: (1) dislocation accumulation; (2) residual martensite. [50,60]. During the repeated loading process, dislocations are generated and accumulated, gradually leading to the activation of dislocation slips instead of MT, which is irrecoverable after unloading [60]. Moreover, some martensite is restricted by the high-volume dislocations, resulting in a smaller ΔT_{ad} in the following cycles. As the number of cycles increases, the dislocation density tends to saturate, leading to a stable volume fraction of active martensite and consequently a consistent elastocaloric response [60]. Nevertheless, the maximum ΔT_{ad} of −12.02 K in S1 alloy in this work is obviously larger than the reported ΔT_{ad} of Cu-based SMAs (4–10 K) and NiMn-based SMA (3–6 K) [61–64].

To quantitatively assess the practical refrigeration potential, we evaluated the refrigeration capacity (RC) using the relationship [65]:

$$RC = \int_{\Delta T_{win}} \Delta S(T)\, dT \tag{4}$$

where ΔS represents the entropy change during stress-induced transformation and ΔT_{win} denotes the working temperature window. This integral, performed over the transformation temperature range shown in Fig. 6 (c), yields RC values of particular significance for actual cooling applications. The calculated RC values reveal that the S2 alloy achieves a great performance with 3.26 kJ/kg, which is greater than the counterparts of S0 with 2.3 kJ/kg and S1 with 1.91 kJ/kg due to their limited working temperature window. The value is also larger than the 2.55 kJ/kg reported for CuAlMn SMAs and the 1.4 kJ/kg for FePd SMAs [66,67].

It should be mentioned that the commercial application of elastocaloric materials typically requires high fatigue resistance and a stable functional stability (over 10^7 cycles) [2]. While the high fatigue performance of NiTiNb SMAs is beyond the scope of this work, more comprehensive research should be conducted in the future to improve their functional stability. Previously successful approaches for achieving stable functional performance in SMAs with nanocrystalline matrix or heterogeneous structure could also be applied in ternary NiTiNb SMAs to enhance fatigue resistance [68,69]. In conclusion, the comprehensive results confirm that the developed NiTiNb alloys simultaneously satisfy three essential requirements for practical elastocaloric refrigeration: (1) large adiabatic temperature changes, (2) wide working temperature windows, and (3) high refrigeration capacity. The S2 alloy in particular demonstrates outstanding overall performance, especially in a wider working temperature window, making it a highly promising candidate for solid-state cooling applications that demand both large cooling power and a broad working temperature window.

4. Conclusions

In this study, we systematically investigated the microstructure, phase transformation behavior, superelastic properties, and elastocaloric performance of $Ni_{50.8-x}Ti_{49.2}Nb_x$ ($x = 0, 1, 2, 3$) SMAs. The experimental results confirm that Nb-doped NiTi SMAs, with an optimal combination of significant adiabatic temperature changes and a wide working temperature window, are promising candidates for solid-state refrigeration applications. The composition-dependent functional properties optimization achieved in this work provides a guideline for developing next-generation elastocaloric materials tailored for specific cooling applications. The following conclusions are drawn.

(1) The Ni_4Ti_3 precipitates were found in the S0 sample after aging treatment, while it was not found in aged Nb-doped S1–S3 samples. Instead, the Nb-rich dendrite and eutectic β-Nb phase were observed in aged Nb-doped samples.
(2) The addition of Nb effectively suppresses thermal-induced MT through stabilization of the parent phase, resulting in a significant reduction in MT temperatures and an increase in thermal hysteresis.
(3) The critical stress for stress-induced MT and the corresponding transition strain increased substantially from 248.41 MPa to 4.08 % of the aged S0 alloy to 889.11 MPa and 4.46 % of the aged S2 alloy.
(4) While all samples exhibited large ΔT_{ad} during stress loading-unloading cycles, the S1 alloy showed superior elastocaloric performance with a ΔT_{ad} of -11.97 K at RT and of -12.02 K at PT.
(5) The S2 alloy demonstrated great functional properties, exhibiting a working temperature window exceeding 100 K (theoretically 118.84 K) for both superelastic and elastocaloric effects and a large refrigeration capacity with 3.26 kJ/kg. This remarkable temperature window arises from the synthesis of parent-phase stabilization and enhanced yield strength of the parent phase through Nb-induced strengthening mechanisms.

CRediT authorship contribution statement

Bailiang Qin: Validation, Investigation, Visualization, Writing – original draft. Ze Pu: Writing – review & editing. Changyong Chen: Writing – review & editing. Yongyun Zhang: Writing – review & editing. K. C. CHAN: Conceptualization, Methodology, Resources, Validation, Writing – review & editing, Supervision, Project administration, Funding acquisition.

Declaration of competing interest

The authors declare that they have no known competing financial interests or personal relationships that could have appeared to influence the work reported in this paper.

Acknowledgement

This work was supported by a grant from the Research Institute of Advanced Manufacturing of The Hong Kong Polytechnic University (project code: 1-CD8Y).

Data availability

The raw/processed data required to reproduce these findings cannot be shared at this time, as the data also forms part of an ongoing study.

References

[1] Lloveras P, Stern-Taulats E, Barrio M, Tamarit JL, Crossley S, Li W, Pomjakushin V, Planes A, Manosa L, Mathur ND, Moya X. Giant barocaloric effects at low pressure in ferrielectric ammonium sulphate. Nat Commun 2015;6:8801.
[2] Tušek J, Engelbrecht K, Millán-Solsona R, Mañosa L, Vives E, Mikkelsen LP, Pryds N. The elastocaloric effect: a way to cool efficiently. Adv Energy Mater 2015; 5(13).
[3] Moya X, Kar-Narayan S, Mathur ND. Caloric materials near ferroic phase transitions. Nat Mater 2014;13(5):439–50.
[4] Qian S, Geng Y, Wang Y, Ling J, Hwang Y, Radermacher R, Takeuchi I, Cui J. A review of elastocaloric cooling: materials, cycles and system integrations. Int J Refrig 2016;64:1–19.
[5] Tušek J, Engelbrecht K, Eriksen D, Dall'Olio S, Tušek J, Pryds N. A regenerative elastocaloric heat pump. Nat Energy 2016;1(10).
[6] Gottschall T, Benke D, Fries M, Taubel A, Radulov IA, Skokov KP, Gutfleisch O. A Matter of Size and Stress: Understanding the First-Order Transition in Materials for Solid-State Refrigeration. Adv Func Mater 2017;27(32).
[7] Imran M, Zhang X. Recent developments on the cyclic stability in elastocaloric materials. Mater Des 2020;195.
[8] Bonnot E, Romero R, Manosa L, Vives E, Planes A. Elastocaloric effect associated with the martensitic transition in shape-memory alloys. Phys Rev Lett 2008;100 (12):125901.
[9] Zhang G, Wang H, Li Z, Yang B, Yan H, Zhao X, Zuo L. Colossal elastocaloric effect in a <001>A oriented Ni49Mn33Ti18 polycrystalline alloy. Scr Mater 2023;234.
[10] Masdeu F, Pons J, Torrens-Serra J, Chumlyakov Y, Cesari E. Superelastic behavior and elastocaloric effect in a Ni51.5Fe21.5Ga27.0 ferromagnetic shape memory single crystal under compression. Mater Sci Eng, A 2022;833.
[11] Lu N-H, Chen C-H. Compressive stress-induced martensitic transformation and elastocaloric effect in Cu-Al-Mn single-crystal alloy. Mater Sci Eng, A 2022;840.
[12] Pataky GJ, Ertekin E, Sehitoglu H. Elastocaloric cooling potential of NiTi, Ni2FeGa, and CoNiAl. Acta Mater 2015;96:420–7.
[13] Sehitoglu H, Wu Y, Ertekin E. Elastocaloric effects in the extreme. Scr Mater 2018; 148:122–6.
[14] Tušek J, Engelbrecht K, Mikkelsen LP, Pryds N. Elastocaloric effect of Ni-Ti wire for application in a cooling device. J Appl Phys 2015;117(12).
[15] Cui J, Wu Y, Muehlbauer J, Hwang Y, Radermacher R, Fackler S, Wuttig M, Takeuchi I. Demonstration of high efficiency elastocaloric cooling with large ΔT using NiTi wires. Appl Phys Lett 2012;101(7).
[16] Imran M, Zhang X. Reduced dimensions elastocaloric materials: a route towards miniaturized refrigeration. Mater Des 2021;206.
[17] Wang D, Hou S, Wang Y, Ding X, Ren S, Ren X, Wang Y. Superelasticity of slim hysteresis over a wide temperature range by nanodomains of martensite. Acta Mater 2014;66:349–59.
[18] Li Z, Li Z, Li D, Yang J, Yang B, Hu Y, Wang D, Zhang Y, Esling C, Zhao X, Zuo L. Achieving a broad refrigeration temperature region through the combination of successive caloric effects in a multiferroic Ni50Mn35In15 alloy. Acta Mater 2020; 192:52–9.
[19] Hou H, Simsek E, Stasak D, Hasan NA, Qian S, Ott R, Cui J, Takeuchi I. Elastocaloric cooling of additive manufactured shape memory alloys with large latent heat. J Phys Appl Phys 2017;50(40).
[20] Chen Y, Tyc O, Molnárová O, Heller L, Šittner P. Tensile deformation of superelastic NiTi wires in wide temperature and microstructure ranges. Shape Memory Superelasticity 2018;5(1):42–62.
[21] Li S, Cong D, Sun X, Zhang Y, Chen Z, Nie Z, Li R, Li F, Ren Y, Wang Y. Wide-temperature-range perfect superelasticity and giant elastocaloric effect in a high entropy alloy. Mater Res Lett 2019;7(12):482–9.
[22] Dang P, Zhang L, Zhou Y, Liang Q, Ding X, Sun J, Xue D. Cryogenic superelasticity and elastocaloric effect in a nanostructured Ti-Ni-Co alloy. Scr Mater 2023;236.
[23] Wang D, Zhang Z, Zhang J, Zhou Y, Wang Y, Ding X, Wang Y, Ren X. Strain glass in Fe-doped Ti–Ni. Acta Mater 2010;58(18):6206–15.
[24] Zhou Y, Xue D, Ding X, Wang Y, Zhang J, Zhang Z, Wang D, Otsuka K, Sun J, Ren X. Strain glass in doped Ti50(Ni50−xDx) (D=Co, Cr, Mn) alloys: implication for the generality of strain glass in defect-containing ferroelastic systems. Acta Mater 2010;58(16):5433–42.
[25] Liu S, Han S, Zhang L, Chen L-Y, Wang L, Zhang L, Tang Y, Liu J, Tang H, Zhang LC. Strengthening mechanism and micropillar analysis of high-strength NiTi–Nb eutectic-type alloy prepared by laser powder bed fusion. Compos B Eng 2020;200.
[26] Bao ZZ, Guo S, Xiao F, Zhao XQ. Development of NiTiNb in-situ composite with high damping capacity and high yield strength. Prog Nat Sci Mater Int 2011;21(4): 293–300.
[27] Shi H, Frenzel J, Martinez GT, Van Rompaey S, Bakulin A, Kulkova S, Van Aert S, Schryvers D. Site occupation of Nb atoms in ternary Ni–Ti–Nb shape memory alloys. Acta Mater 2014;74:85–95.

[28] Fan QC, Zhang Y, Zhang YH, Wang YY, Yan EH, Huang SK, Wen YH. Influence of Ni/Ti ratio and Nb addition on martensite transformation behavior of NiTiNb alloys. J Alloys Compd 2019;790:1167–76.

[29] Hao S, Cui L, Jiang D, Han X, Ren Y, Jiang J, Li J. A transforming metal nanocomposite with large elastic strain, low modulus, and high strength. Science 2013;339(6124):1191–4.

[30] Zhang Y, Liu J, Wang L, Wei D, Liu C, Wang K, Tang Y, Zhang L, Lu W. Porous NiTiNb alloys with superior strength and ductility induced by modulating eutectic microregion. Acta Mater 2022;239.

[31] Wang L, Xie L, Zhang LC, Chen L, Ding Z, Lv Y, Zhang W, Lu W, Zhang D. Microstructure evolution and superelasticity of layer-like NiTiNb porous metal prepared by eutectic reaction. Acta Mater 2018;143:214–26.

[32] Xi R, Jiang H, Li G, Zhang Z, Wei H, Zhao G, Humbeeck JV, Wang X. Effect of solution treatment on the microstructure, phase transformation behavior and functional properties of NiTiNb ternary shape memory alloys fabricated via laser powder bed fusion in-situ alloying. Int J Extrem Manuf 2024;6(4).

[33] Xi R, Jiang H, Li G, Kustov S, Zhang Z, Wei H, Liu Z, Zhao G, Van Humbeeck J, Wang X. In-situ alloying of NiTiNb ternary shape memory alloys via laser powder bed fusion using pre-alloyed NiTi and elemental Nb powders: microstructure, phase transformation behavior and functional properties. Addit Manuf 2024;79.

[34] Xi R, Jiang H, Kustov S, Zhang Z, Zhao G, Vanmeensel K, Van Humbeeck J, Wang X. Influence of Nb addition and process parameters on the microstructure and phase transformation behavior of NiTiNb ternary shape memory alloys fabricated by laser powder bed fusion. Scr Mater 2023;222.

[35] Ying C, Hai-chang J, Li-jian R, Li X, Xin-qing Z. Mechanical behavior in NiTiNb shape memory alloys with low Nb content. Intermetallics 2011;19(2):217–20.

[36] Wang M, Jiang M, Liao G, Guo S, Zhao X. Martensitic transformation involved mechanical behaviors and wide hysteresis of NiTiNb shape memory alloys. Prog Nat Sci Mater Int 2012;22(2):130–8.

[37] Otsuka K, Ren X. Physical metallurgy of Ti–Ni-based shape memory alloys. Prog Mater Sci 2005;50(5):511–678.

[38] Pu Z, Du D, Zhang D, Li Z, Xue S, Xi R, Wang X, Chang B. Improvement of tensile superelasticity by aging treatment of NiTi shape memory alloys fabricated by electron beam wire-feed additive manufacturing. J Mater Sci Technol 2023;145: 185–96.

[39] Lv C, Wang K, Wang B, Zheng J, Zhang K, Li G, Lai Y, Fu Y, Hou H, Zhao X. Coexistence of strain glass transition and martensitic transformation in highly nickel-rich ferroelastic alloy with large elastocaloric effect. Acta Mater 2024;264.

[40] Liang X, Xiao F, Chen H, Li Z, Li Z, Jin X, Fukuda T. Internal friction of the R-phase in single crystalline Ti-50.8Ni (at.%) alloy containing controlled precipitate of Ti3Ni4. Scr Mater 2019;166:44–7.

[41] Wang XB, Verlinden B, Van Humbeeck J. R-phase transformation in NiTi alloys. Mater Sci Technol 2014;30(13):1517–29.

[42] Khalil-Allafi J, Dlouhy A, Eggeler G. Ni4Ti3-precipitation during aging of NiTi shape memory alloys and its influence on martensitic phase transformations. Acta mater 2002;50(17):4255–74.

[43] Fan QC, Sun MY, Zhang YH, Wang YY, Zhang Y, Peng HB, Sun KH, Fan XH, Huang SK, Wen YH. Influence of precipitation on phase transformation and mechanical properties of Ni-rich NiTiNb alloys. Mater Char 2019;154:148–60.

[44] Frenzel J, George EP, Dlouhy A, Somsen C, Wagner MFX, Eggeler G. Influence of Ni on martensitic phase transformations in NiTi shape memory alloys. Acta Mater 2010;58(9):3444–58.

[45] Isomäki I, Hämäläinen M, Gasik M. Thermodynamic assessment of the ternary Ni–Ti–Cr system. J Alloys Compd 2012;543:12–8.

[46] Otsuka CMWK. Shape memory materials. London: Cambridge University Press; 1998.

[47] Yin H, Ma G, Fan Q, Wang Y, Huang S, Yi Y. Thermal-Induced phase transformation behavior of NiTiNb hypoeutectic, eutectic, and hypereutectic alloys. Metals 2019;9 (2).

[48] Kang G, Zhang H, Ma Z, Ren Y, Cui L, Yu K. Large thermal hysteresis in a single-phase NiTiNb shape memory alloy. Scr Mater 2022;212.

[49] Zhao X, Yan X, Yang Y, Xu H. Wide hysteresis NiTi(Nb) shape memory alloys with low Nb content (4.5at.%). Mater Sci Eng, A 2006;438–440:575–8.

[50] Cao Y, Zhou X, Cong D, Zheng H, Cao Y, Nie Z, Chen Z, Li S, Xu N, Gao Z, Cai W, Wang Y. Large tunable elastocaloric effect in additively manufactured Ni–Ti shape memory alloys. Acta Mater 2020;194:178–89.

[51] Yang Z, Cong D, Yuan Y, Li R, Zheng H, Sun X, Nie Ren Y, Wang Y Z. Large room-temperature elastocaloric effect in a bulk polycrystalline Ni-Ti-Cu-Co alloy with low isothermal stress hysteresis. Appl Mater Today 2020;21:100844.

[52] Wu Y, Ertekin E, Sehitoglu H. Elastocaloric cooling capacity of shape memory alloys – role of deformation temperatures, mechanical cycling, stress hysteresis and inhomogeneity of transformation. Acta Mater 2017;135:158–76.

[53] Waitz T, Kazykhanov V, Karnthaler HP. Martensitic phase transformations in nanocrystalline NiTi studied by TEM. Acta Mater 2004;52(1):137–47.

[54] Ossmer H, Miyazaki S, Kohl M. The elastocaloric effect in TiNi-based foils. Mater Today Proc 2015;2:S971–4.

[55] Xiao Y, Zeng P, Lei L, Zhang Y. In situ observation on temperature dependence of martensitic transformation and plastic deformation in superelastic NiTi shape memory alloy. Mater Des 2017;134:111–20.

[56] Saghaian SM, Karaca H, Tobe H, Souri M, Noebe R, Chumlyakov YI. Effects of aging on the shape memory behavior of Ni-rich Ni50. 3Ti29 7Hf20 single crystals 2015; 87:128–41.

[57] Liu Y, Galvin SP. Criteria for pseudoelasticity in near-equiatomic NiTi shape memory alloys 1997;45(11):4431–9.

[58] Zhang H, Liu J, Ma Z, Ren Y, Jiang D, Cui L, Yu K. Small stress-hysteresis in a nanocrystalline TiNiCuFe alloy for elastocaloric applications over wide temperature window. J Alloys Compd 2022;928.

[59] Bonnot E, Romero R, Mañosa L, Vives E, Planes A. Elastocaloric effect associated with the martensitic transition in shape. Memory Alloys 2008;100(12):125901.

[60] Yang Z, Cong DY, Sun XM, Nie ZH, Wang YD. Enhanced cyclability of elastocaloric effect in boron-microalloyed Ni-Mn-In magnetic shape memory alloys. Acta Mater 2017;127:33–42.

[61] Li D, Li Z, Zhang X, Yang B, Wang D, Zhao X, Zuo L. Enhanced cyclability of elastocaloric effect in a directionally solidified Ni55Mn18Ga26Ti1 alloy with low hysteresis. Scr Mater 2020;189:78–83.

[62] Yuan B, Zhong S, Qian M, Zhang X, Geng L. Elastocaloric effect in bamboo-grained Cu71.1Al17.2Mn11.7 microwires. J Alloys Compd 2021;850.

[63] Niitsu K, Kimura Y, Omori T, Kainuma R. Cryogenic superelasticity with large elastocaloric effect. NPG Asia Mater 2018;10(1):e457. e457.

[64] Cheng P, Zhou Z, Chen J, Li Z, Yang B, Xu K, Li Z, Li J, Zhang Z, Wang D, Qian S, Du Y. Combining magnetocaloric and elastocaloric effects in a Ni45Co5Mn37In13 alloy. J Mater Sci Technol 2021;94:47–52.

[65] Gschneidner KA, Pecharsky V, Tsokol AO. Recent developments in magnetocaloric materials. Reports on progress in physics 2005;68(6):1479.

[66] Xu S, Huang HY, Xie J, Takekawa S, Xu X, Omori T, Kainuma R. Giant elastocaloric effect covering wide temperature range in columnar-grained Cu71.5Al17.5Mn11 shape memory alloy. APL Mater 2016;4(10).

[67] Nikitin S, Myalikgulyev G, Annaorazov M, Tyurin A, Myndyev R, Akopyan S. Giant elastocaloric effect in FeRh alloy. Phys Lett 1992;171(3–4):234–6.

[68] Hou H, Simsek E, Ma T, Johnson NS, Qian S, Cisse C, Stasak D, Al Hasan N, Zhou L, Hwang Y, Radermacher R, Levitas VI, Kramer MJ, Zaeem MA, Stebner AP, Ott RT, Cui J, Takeuchi I. Fatigue-resistant high-performance elastocaloric materials made by additive manufacturing. Science 2019;366(6469):1116–21.

[69] Chen H, Xiao F, Liang X, Li Z, Jin X, Fukuda T. Stable and large superelasticity and elastocaloric effect in nanocrystalline Ti-44Ni-5Cu-1Al (at%) alloy. Acta Mater 2018;158:330–9.